

Physically Consistent and Efficient Variational Denoising of Image Fluid Flow Estimates

Andrey Vlasenko and Christoph Schnörr

Abstract—Imaging plays an important role in experimental fluid dynamics. It is equally important both for scientific research and a range of industrial applications. It is known, however, that estimated velocity fields of fluids often suffer from various types of corruptions like missing data, for instance, that make their physical interpretation questionable. We present an algorithm that accepts a wide variety of corrupted 2-D vector fields as input data and allows to recover missing data fragments and to remove noise in a physically plausible way. Our approach essentially exploits the physical properties of incompressible fluid flows and does not rely upon any particular model of noise. As a result, the developed algorithm performs well and robust for different types of noise and estimation errors. The computational algorithm is sufficiently simple to scale up to large 3-D problems.

Index Terms—Experimental fluid mechanics, image sequence processing, incompressible flows, particle image velocimetry, variational motion estimation.

I. INTRODUCTION

EXPERIMENTAL fluid mechanics is a challenging field of research of imaging science with important industrial applications [1]. During the last two decades, the prevailing technique for investigating turbulent flows through imaging has been *Particle image velocimetry (PIV)* in 2-D [3], [4], whereas various 3-D measurement techniques, while being attractive from the physical viewpoint of applications, have been suffering from various drawbacks including noisy measurements, complexity and costs of the set-up, and limited resolution [6], [8]–[12]. Remarkable progress has been recently achieved through a novel technique, Tomographic Particle Image Velocimetry (TomoPIV) [13] that, in principle, provides 3-D estimates with higher spatial resolution.

As a result of this previous research, there is a range of methods for computing vector field estimates of incompressible viscous flows from image data, that exhibit diverse artifacts depending on the particular technique used, and on the particular physical scenario considered. For example, too low local densities of particles in PIV experiments may lead to local regions

with missing vector field estimates. Very high local particle densities, on the other hand, hampers correspondence analysis and may result in erroneous local vector field estimates. This motivates to investigate a method that denoises a given vector field in a *physically plausible* way, and independently of the method that was used to estimate the velocity field from image data. Therefore, rather than to model noise explicitly which is difficult and too specific due to the diversity of estimation errors that can occur, the method should return a vector field that is close to the input data and approximately satisfies the basic physical equations governing the flow. At the same time, the method should be robust to various types of estimation errors and computationally simple, so as to be applicable to large-scale 3-D problems that the next generation of 3-D measurement techniques will raise in the near future.

Our approach presented below is motivated by recent work on *variational* methods applied to fluid estimation and PIV [14]–[16], in particular those employing physically motivated regularization. Ruhnau and Schnörr [19] showed how to estimate *physically consistent* flow from PIV image sequences utilizing a distributed-parameter control approach. This idea has been extended in [20] to a dynamic setting based on the vorticity transport equation formulation of the Navier-Stokes equation.

The task studied in this paper is more involved, however, because we wish to process corrupted vector fields as input data, and, therefore, cannot resort to image data in order to determine additional control variables as in [19], for example. Rather, we wish to devise a method that accepts vector field estimates produced by *any* algorithm [1], [4], and returns a denoised version just by preserving and enforcing physically consistent flow structure.

The paper is organized as follows. The approach comprises several stages that will be presented and discussed in Section II. The applicability of the developed methodology is demonstrated by a range of experiments and discussed in Section III. The basic findings are summarized in Section V.

II. APPROACH

Notation: $\mathbf{v} = (v_1, v_2)^\top$ denotes a 2-D velocity field. All vectors will hereafter appear in bold font. $\nabla := ((\partial/\partial x_1)(\partial/\partial x_2))^\top$ denotes the nabla operator and $\nabla \cdot \mathbf{v}$ the divergence of \mathbf{v} . The curl operator $\nabla \times$ is used in this paper in two ways. For any vector field $\mathbf{f}: \mathbf{x} \rightarrow (f_1, f_2)^\top$, $\mathbf{x} = (x_1, x_2)^\top \in \Omega \subset \mathbb{R}^2$ (image domain), we define its vorticity field as $\nabla \times \mathbf{f} := \partial_{x_1} f_2 - \partial_{x_2} f_1$, which is a scalar field. In particular, the vorticity of the velocity field \mathbf{v} is denoted with $\omega = \nabla \times \mathbf{v}$. For any scalar field $\psi: \mathbf{x} \rightarrow \mathbb{R}$, taking

Manuscript received October 14, 2008; revised October 14, 2009. First published November 20, 2009; current version published February 18, 2010. This work was supported by the German Science Foundation (DFG) within the priority research program 1147, “Image Measurements in Experimental Fluid Mechanics”, under grant SCHN 457/9-3. The associate editor coordinating the review of this manuscript and approving it for publication was Prof. Scott T. Acton.

The authors are with the University of Heidelberg, Department Mathematics and Computer Science, Image and Pattern Analysis Group (IPA), and the Heidelberg Collaboratory for Image Processing (HCI), Germany (e-mail: vlasenko@math.uni-heidelberg.de; schnoerr@math.uni-heidelberg.de).

Digital Object Identifier 10.1109/TIP.2009.2036673

the curl returns the vector field $\nabla \times \psi = (\partial_{x_2} \psi, -\partial_{x_1} \psi)^\top$. Applying the curl operator twice results in the Laplacian

$$\nabla \times \nabla \times \omega = -\Delta \omega. \quad (1)$$

The Euclidean inner product and a norm are denoted by $\langle \mathbf{u}, \mathbf{v} \rangle$ and $\|\mathbf{v}\|$, respectively, whereas $\langle \mathbf{u}, \mathbf{v} \rangle_\Omega, \|\mathbf{v}\|_\Omega$ denote the inner product and norm of $[L^2(\Omega)]^2$. In addition, fluid flows are assumed to be incompressible, i.e.,

$$\nabla \cdot \mathbf{v} = 0. \quad (2)$$

It is known that the dynamics of incompressible fluid is governed by the *vorticity-transport equation (VTE)*

$$\frac{\partial}{\partial t} \omega + (\mathbf{v} \cdot \nabla) \omega = \nu \Delta \omega \quad (3)$$

where ν denotes the viscosity coefficient. It will be convenient to use a shorthand for the left hand side of the VTE

$$e(\mathbf{v}) = \nu \Delta \omega, \quad e(\mathbf{v}) := \frac{\partial \omega}{\partial t} + (\mathbf{v} \cdot \nabla) \omega. \quad (4)$$

Finally, the identity

$$\langle \nabla \times \mathbf{v}, \phi \rangle_\Omega - \langle \mathbf{v}, \nabla \times \phi \rangle_\Omega = 0, \quad \forall \phi \in C_0^1(\Omega) \quad (5)$$

is valid for smooth functions ϕ with compact support.

A. Overview Over the Approach

Suppose we have given a corrupted velocity field \mathbf{d} . It is convenient to consider \mathbf{d} as comprising two components, $\mathbf{d} = \mathbf{u} + \mathbf{v}_n$. The first component \mathbf{u} satisfies the continuum mechanics (2)–(3) and is hereafter referred to as true fluid flow estimate. The second component \mathbf{v}_n does not satisfy the hydrodynamics equations and is considered as noise. Note that “noise” is not explicitly defined but rather in a broad way as nonphysical flows. The problem is to estimate \mathbf{u} from \mathbf{d} in a computational efficient way. Our approach comprises the following four steps that will be detailed in subsequent sections.

- 1) Remove the divergence from \mathbf{d} by projection onto the linear subspace of incompressible vector fields $\{\mathbf{v} \mid \nabla \cdot \mathbf{v} = 0\}$.
- 2) Remove noise by Gaussian low-pass filtering.
- 3) Compute the vorticity $\omega_{\mathbf{v}} = \nabla \times \mathbf{v}$ and enforce physically plausible flow structure in terms of a vorticity field ω satisfying the VTE (4).
- 4) Recover an incompressible velocity field \mathbf{u} from the vorticity field ω .

This algorithm is a modified and computationally more efficient version of the procedure announced in [2]. The modification consists in replacing iterative application of a linear diffusion operator at Step 2 by Gaussian filtering with a carefully selected scale, resulting in much more efficient computations without loss of accuracy. In addition, incompressibility is not only considered in step 1, but in step 4 as well. As a consequence, it turned out that satisfying restorations can be obtained by a single pass, that is by applying these steps only once. This is a significant advantage not only for 2-D applications but also in view of large 3-D data sets to be expected in the near future, cf. [13]. We consider next each of the above steps in turn.

B. Solenoidal Projection

Let the image domain $\Omega \subset \mathbb{R}^2$ be simply-connected. Then the following orthogonal decomposition of vector fields holds [17]

$$[L^2(\Omega)]^2 = \nabla H_0^1(\Omega) \oplus H(\text{div}0; \Omega) \quad (6)$$

where $H_0^1(\Omega)$ denotes the subspace of $L^2(\Omega)$ of functions with square-integrable first-order derivatives and vanishing boundary values, and $H(\text{div}0; \Omega)$ denotes the subspace of divergence-free vector fields. Given a divergent vector field $\mathbf{d} \in [L^2(\Omega)]^2$, we compute the decomposition $\mathbf{d} = \nabla p + \mathbf{v}$ according to (6) as follows. Applying the divergence operator to \mathbf{v} gives

$$\nabla \cdot \mathbf{v} = \nabla \cdot \mathbf{d} - \Delta p = 0 \quad (7)$$

and, hence, a Dirichlet problem for p

$$\Delta p = \nabla \cdot \mathbf{d} \quad \text{in } \Omega \quad (8a)$$

$$p = 0 \quad \text{on } \partial \Omega. \quad (8b)$$

Substituting p into $\mathbf{v} = \mathbf{d} - \nabla p$ results in the divergence-free flow \mathbf{v} .

Having computed \mathbf{v} , we continue removing noise by lowpass filtering in a subsequent step.

C. Lowpass Filtering

An incompressible turbulent fluid flow can be considered as a superposition of eddies at various scales (see Fig. 3). Let λ be the size of a vortex, ϵ the average dissipation energy, and $k \propto 1/\lambda$ the corresponding wave number. Theory [18] suggests that the energy spectrum of homogeneous turbulence obeys the law $v_\lambda^2 \sim (\epsilon/k)^{2/3}$ with the most significant part of energy concentrated at small wavenumbers k . If the data set is corrupted by some noise, produced either by measurements or data processing, the spectral characteristics differ, especially at larger wavenumbers k . Fig. 1 depicts such a typical spectrum. For comparison, the spectrum of a flow \mathbf{d} corrupted by “white” noise is also shown.

Fig. 1 suggests that a considerable amount of noise can be simply removed by lowpass filtering. While sophisticated filtering schemes employing a multiscale expansion of the flow [7] are conceivable, we will show below that simple Gaussian low-pass filtering in conjunction with the other three steps of our overall approach (cf. Section II-B), works fine. We only have to choose a conservative cutoff-frequency that is large enough so as not to damage physically significant structures of the flow.

Denoting the impulse response and its Fourier transform by

$$g_\sigma(\mathbf{x}) = \frac{1}{2\pi\sigma^2} \exp\left(-\frac{1}{2\sigma^2} \|\mathbf{x}\|^2\right) \quad (9a)$$

$$\hat{g}_\sigma(\mathbf{w}) = \exp\left(-\frac{\sigma^2}{2} \|\mathbf{w}\|^2\right) \quad (9b)$$

the scale parameter σ is chosen as follows: The smallest vortex size that can be resolved on the computational grid has a size of about 3 pixels, corresponding to the angular wavenumber $2\pi/3$. We empirically choose $\sigma = 1.34$ in (9b) so as to lower the amplitude spectrum at this point by the factor 1/50.

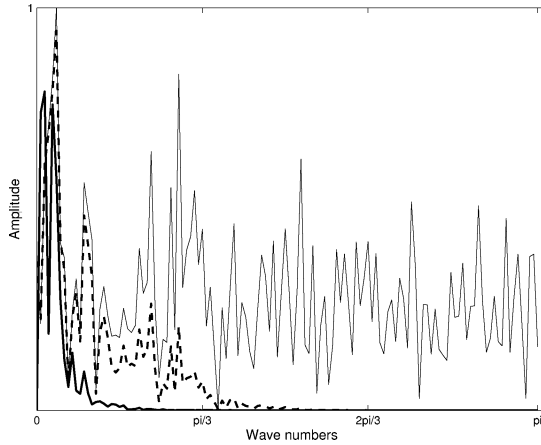


Fig. 1. Velocity spectra of an original turbulent fluid flow (thick solid line), the flow corrupted by noise (fine solid line), and the flow after solenoidal projection (8), (7) and Gaussian lowpass filtering (10) (dashed line). Although noise has been effectively removed, a significant nonphysical component of the fluid flow estimate remains—cf. Fig. 2, bottom, and Fig. 3, top.

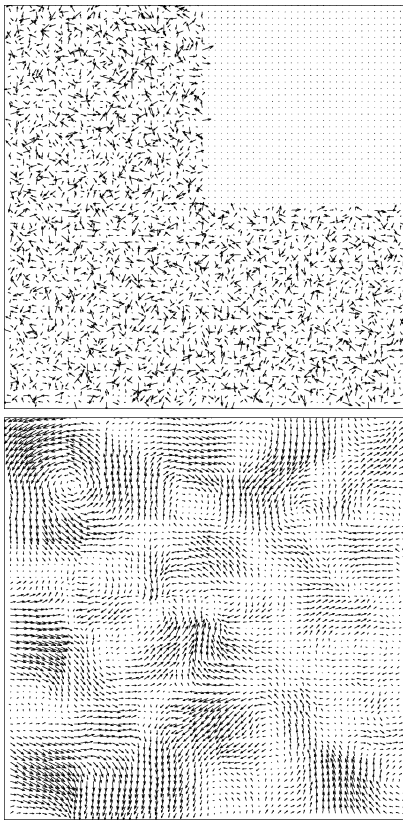


Fig. 2. Top panel: Noisy input field. The original data field without noise is shown in the upper right quadrant to illustrate the signal-to-noise ratio. Bottom panel: The data field after filtering using the Gaussian filter. Although noise has been effectively removed, a significant nonphysical component of the fluid flow estimate remains—cf. Fig. 3, top.

Fig. 1 shows the amplitude spectrum of the smoothed flow (* denotes convolution)

$$\mathbf{v}_g = g_\sigma * \mathbf{v} \quad (10)$$

as a dashed line. This result indicates that our choice $\sigma = 1.34$ is conservative in that it does not affect the “true” spectrum. On

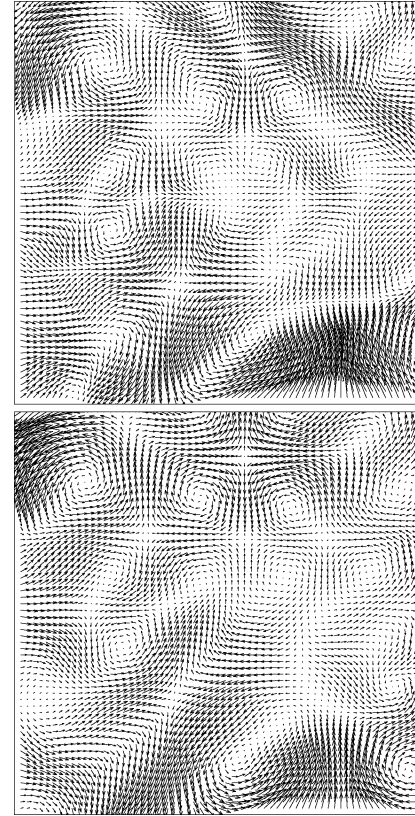


Fig. 3. Top panel: Restored flow corresponding to Fig. 2 but after the complete cycle of four computational steps of the overall approach. Bottom panel: Ground truth vector field.

the other hand, despite having effectively removed noise (see Fig. 2), it is also obvious that a significant nonphysical noise component remains – compare Fig. 2, bottom, and Fig. 3, top.

It is important note at this point that up to the boundary $\partial\Omega$, low-pass filtering will not affect the result of the preceding step 1 (solenoidal projection) because $\nabla \cdot \mathbf{v}_g = g_\sigma * \nabla \cdot \mathbf{v} = 0$ as the representation in the Fourier domain shows: $\langle i\mathbf{w}, \hat{\mathbf{v}}_g \rangle = \langle i\mathbf{w}, \hat{g}_\sigma(\mathbf{w})\hat{\mathbf{v}} \rangle = \hat{g}_\sigma(\mathbf{w})\langle i\mathbf{w}, \hat{\mathbf{v}} \rangle$. The way for further improving the velocity estimate becomes clear if we take into account that \mathbf{v}_g in (10) does not satisfy the equations governing incompressible fluids. The consequences will be considered in two subsequent computational steps, to be described next, that will complement the overall approach.

D. Vorticity Rectification

In order to enforce physical consistency of the flow (10) computed in the previous step, we compute its vorticity

$$\omega_g := \nabla \times \mathbf{v}_g \quad (11)$$

and enforce consistency with the VTE (4) by minimizing the functional

$$\min_{\omega} \left\{ \|\omega - \omega_g\|_{\Omega}^2 + \alpha \left(\nu \|\nabla \times \omega\|_{\Omega}^2 + 2\langle e(\mathbf{v}_g), \omega \rangle_{\Omega} \right) \right\}. \quad (12)$$

Notice that ω_g and $e(\mathbf{v}_g)$ are evaluated using the flow (10) computed at the previous step.

The rationale behind the approach (12) becomes apparent when inspecting the corresponding Euler-Lagrange equation

$$\omega - \alpha\nu\Delta\omega = \omega_g - \alpha e(\mathbf{v}_g). \quad (13)$$

This is just a linear diffusion equation to be solved for the restored vorticity field ω . The parameter ν is acting here as a natural smoothing process. Rearranging terms

$$\omega = \omega_g - \alpha(e(\mathbf{v}_g) - \nu\Delta\omega) \quad (14)$$

shows that ω corresponds to the ω_g corrected by the residual of the VTE (4).

We point out that for setting up the functional (12), we deliberately omitted the partial derivative $\partial\omega/\partial t$ in (3). This corresponds to the assumption that this term is negligible relative to the other terms which holds for quasi-stationary flow and flows with large-scale vortices. As a result, we just need a single fluid flow estimate at a single point of time. Experiments in Section II-F below will illustrate that this simplification appears to be reasonable.

Another important issue concerns boundary conditions. In general, there are two types of boundary conditions corresponding to "liquid" and "rigid" boundaries. In the simple case of solid wall or any other rigid contour, all velocity components are equal to zero on the boundary. The situation is less evident for the case of liquid boundaries when there is no obstacle preventing penetration of the fluid through the boundary. If the liquid boundary of the calculational domain coincides with the streamline (e.g., at borders of a convective cell), however, one can set to zero the normal velocity component (so-called slip conditions). The problem is more involved in case of "transparent" fluid boundaries that do not coincide with any streamline so that the flow characteristics on this contour is unknown. For simplicity, we then adopt the *natural* boundary conditions (\mathbf{n} is the unit outer normal at the boundary $\partial\Omega$)

$$\frac{\partial\omega}{\partial\mathbf{n}} = 0 \quad (15)$$

corresponding to the variational problem (12). This, of course, may be only a crude approximation for some real scenarios and lead to the loss of some small-scale flow details.

E. Velocity Restoration

The final step is to convert the restored vorticity field ω back to a velocity field \mathbf{u} . This is accomplished by minimizing

$$\min_{\mathbf{u}} \left\{ \|\mathbf{u} - \mathbf{v}_g\|_{\Omega}^2 + \beta \|\nabla \times \mathbf{u} - \omega\|_{\Omega}^2 \right\} \quad (16a)$$

$$\text{subject to } \nabla \cdot \mathbf{u} = 0 \quad (16b)$$

with \mathbf{v}_g and ω computed at the previous steps (10) and (12), respectively.

The result is a velocity field \mathbf{u} that is physically plausible due to the consistency with the vorticity transport equation enforced in the previous step in terms of ω , and due to the incompressibility constraint (16b).

Using (5), system (16) leads to the constrained variational system

$$\langle \mathbf{u}, \boldsymbol{\phi} \rangle_{\Omega} + \beta \langle \nabla \times \mathbf{u}, \nabla \times \boldsymbol{\phi} \rangle_{\Omega} - \langle p, \nabla \cdot \boldsymbol{\phi} \rangle_{\Omega} \quad (17a)$$

$$= \langle \beta \nabla \times \omega + \mathbf{v}_g, \boldsymbol{\phi} \rangle_{\Omega}, \quad p|_{\partial\Omega} = 0, \quad \forall \boldsymbol{\phi} \\ \langle q, \nabla \cdot \mathbf{u} \rangle_{\Omega} = 0, \quad \forall p, \quad q|_{\partial\Omega} = 0. \quad (17b)$$

in terms of \mathbf{u} and a Lagrange multiplier function p , that are discretized using mixed finite elements, as detailed in [5], [19]. A consequence of this discretization is that the resulting discretized saddle-point problem

$$\begin{pmatrix} \mathbf{A} & \mathbf{B}^{\top} \\ \mathbf{B} & \mathbf{0} \end{pmatrix} \begin{pmatrix} \mathbf{u} \\ \mathbf{p} \end{pmatrix} = \begin{pmatrix} \mathbf{b} \\ \mathbf{0} \end{pmatrix} \quad (18)$$

is numerically stable [5]. Specifically, we can eliminate \mathbf{u}

$$\mathbf{u} = \mathbf{A}^{-1}(\mathbf{b} - \mathbf{B}^{\top}\mathbf{p}) \quad (19)$$

and solve the resulting system

$$\mathbf{B}\mathbf{A}^{-1}\mathbf{B}^{\top}\mathbf{p} = \mathbf{B}\mathbf{A}^{-1}\mathbf{b} \quad (20)$$

numerically stable for \mathbf{p} , yielding \mathbf{u} by backsubstitution of \mathbf{p} into (19).

III. DISCUSSION OF NUMERICAL EXPERIMENTS

A. Data and Error Measurements

In this section, we demonstrate the performance of the developed procedure by considering a range of practically relevant scenarios. The experiments were designed to provide both a visual impression of quality and a quantitative evaluation the results computed with the algorithm described in Sections II-C – II-F.

All experiments were carried out according to the following scheme.

- A simulated vector field, obtained as numerical solution to the Navier-Stokes equations, was taken as a ground truth.
- Then noise was added in terms of white Gaussian noise with both high and low signal-to-noise ratio, as well as in terms of rectangular regions with missing or corrupted data *without* assuming these regions to be known.
- The obtained noisy vector field was used as an input data set for the algorithm, and a restored vector fields was computed.
- Finally, the result was quantitatively compared with ground truth.

The quantitative characteristics of the denoising performance were estimated with the following measures:

\mathbf{g} : ground truth flow, \mathbf{d} : corrupted input data

\mathbf{u} : denoised vector field

$$SDR = \frac{\|\mathbf{d} - \mathbf{g}\|_{\Omega}}{\|\mathbf{u} - \mathbf{g}\|_{\Omega}}, \quad ADR = \frac{\|\arccos(\widehat{\mathbf{d}\mathbf{g}})\|_{\Omega}}{\|\arccos(\widehat{\mathbf{u}\mathbf{g}})\|_{\Omega}}$$

$$NDR = \frac{\|\mathbf{d}\|_{\Omega}}{\|\mathbf{g}\|_{\Omega}}, \quad DDR = \frac{\|\mathbf{u}\|_{\Omega}}{\|\mathbf{g}\|_{\Omega}}.$$

The first measure, SDR , is a ratio of error deviations before and after denoising. It gives an overall information about the error reduction. The second measure, ADR , shows the reduction of average angle deviation of the restored vector field relative to ground truth. The two last measures are the ratios of an average length noisy vector and restored vector, respectively, to ground truth. Comparing them gives some additional information about the level of noise in the considered data set before and after applying our approach.

The described procedure is illustrated below in Figs. 4–7 representing three typical situations which can occur in practice: the vector field is contaminated by noise, contains regions where data are missing or has a coarse spatial resolution only. Ground truth vector fields are presented in the bottom panels of Figs. 4–7. The noisy input data are shown in the top panels whereas the denoised vector fields are shown in the middle panels.

B. White Gaussian Noise

Fig. 4 illustrates the application of our approach to the case of white Gaussian noise. A corrupted input vector field \mathbf{d} as shown in the top panel can be obtained, for instance, in the laboratory or in-situ experiments when using very sensitive sensors or an inaccurate data processing method. A high level of noise was, therefore, chosen for this experiment. To illustrate this, the original signal is shown in a rectangular region in the upper right corner of the noisy input field in Fig. 4.

Comparison of the denoised output vector field \mathbf{u} (middle panel) with the ground truth \mathbf{g} (bottom panel) shows that the algorithm recovers the large-scale structures of the flow very well. So, we conclude that the *default* boundary conditions applied here give a reasonable approximation for such structures near the boundaries of the domain. The result demonstrates that quantitative and robust denoising is possible even for high noise-to-signal ratios.

C. Uniform Noise and Missing Data

A significant property of the presented method is that the class of physically admissible signals are modeled rather than noise explicitly. As a result, it also allows to consider as “noise” regions with missing data as Fig. 5 illustrates. This figure shows the application of our approach to a vector field recorded in the laboratory by a PIV method. It is assumed that some regions of the field do not provide any information during the experiment. These regions are shown in the middle panel as black rectangles. The positions of the regions were randomly set and are assumed to be *unknown*. In addition, uniform noise was added to these data.

Comparison of the middle and bottom panels shows that the algorithm successfully recovered most details of the vector field. This concerns not only the originally recorded data but also regions with missing data.

Fig. 6 depicts as grayvalues the absolute deviation from ground truth before and after denoising. The quantitative meaning of the grayvalues is plotted on the right. Note that two *different* scales are used according to the high- and low noise level, respectively. It is interesting to note that even in problematic regions corresponding to the black rectangles with missing data (Fig. 5, middle panel), the deviation drops from

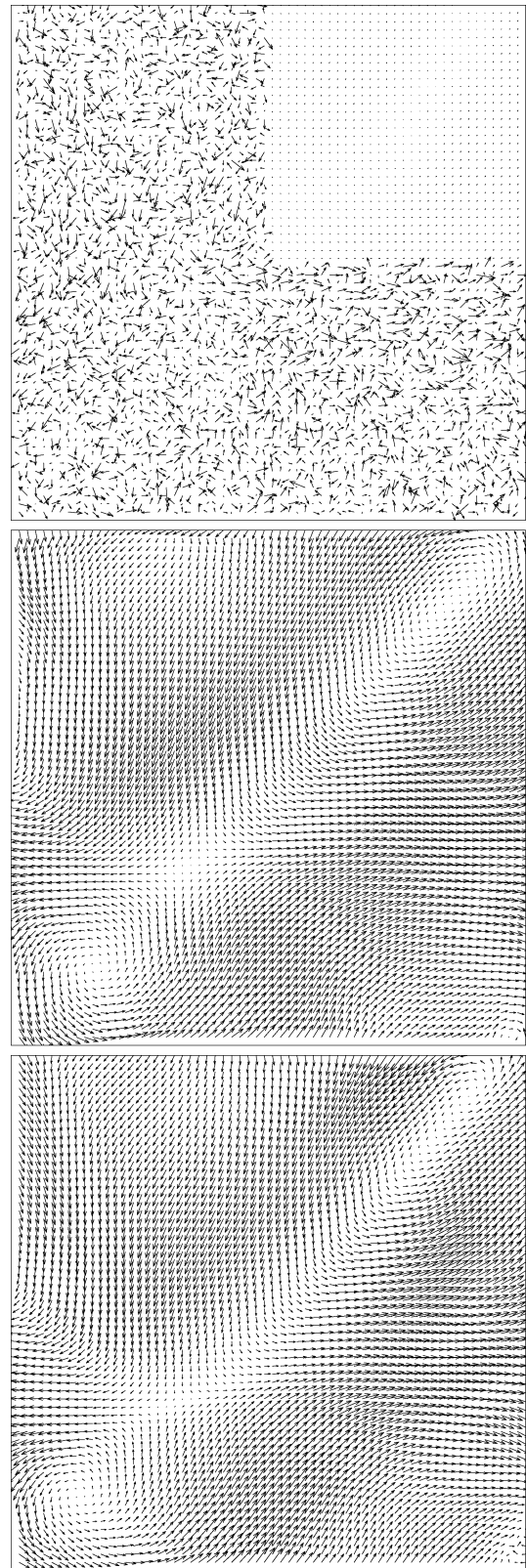


Fig. 4. Top: Noisy input \mathbf{d} . Noise has been cut out within a rectangular region to illustrate the signal-to-noise ratio. Middle: Denoised data \mathbf{u} . Bottom: Ground truth flow \mathbf{g} . Performance measures: $SDR = 4.34$, $ADR = 3.046$, $NDR = 2.12$, $DDR = 0.82$.

about 0.7 (Fig. 6, top panel) to less than 0.2 (Fig. 6, bottom panel).

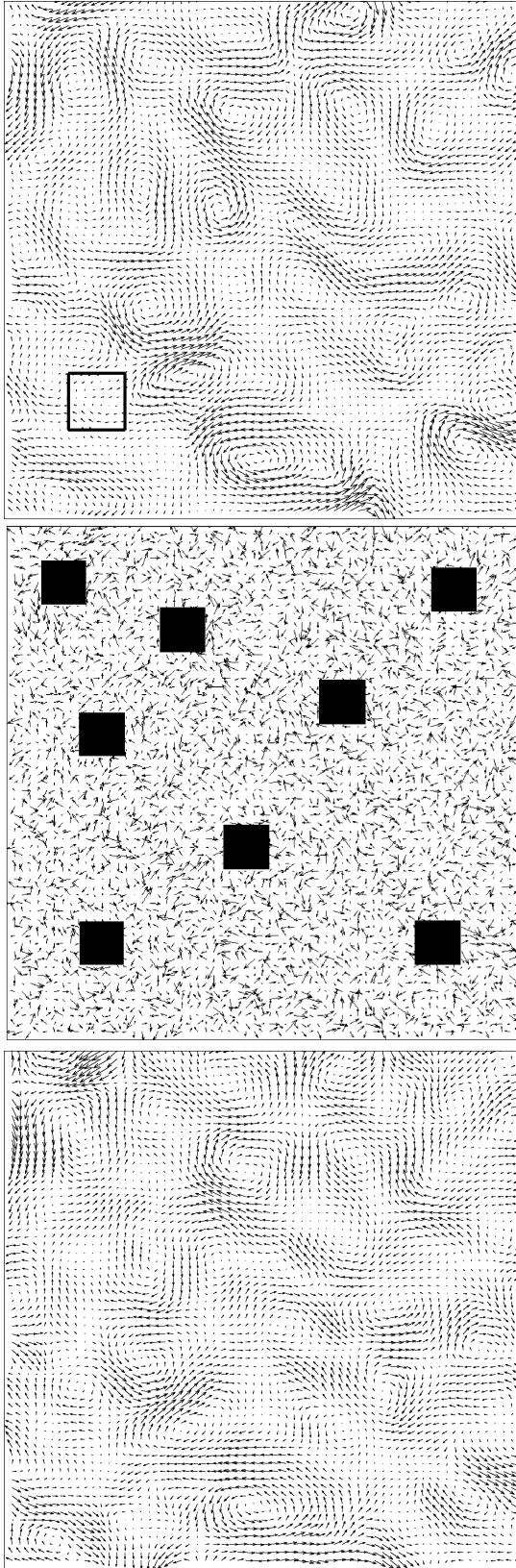


Fig. 5. Top: Ground truth flow \mathbf{g} . Middle: Corrupted data \mathbf{d} by missing values or outliers within rectangular regions. The locations of these regions are assumed to be *unknown*. Bottom: Restored vector field \mathbf{u} . Performance measures: SDR = 3.90, ADR = 3.7, NDR = 2.48, DDR = 0.88.

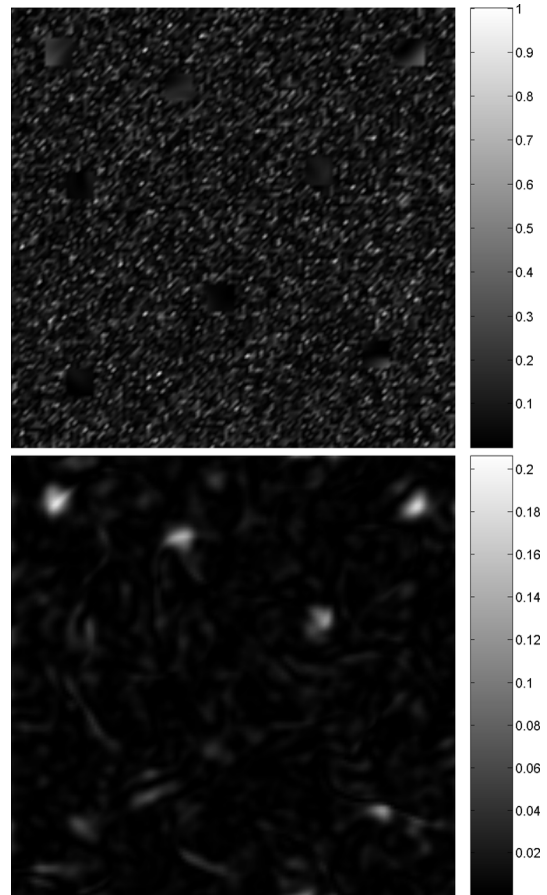


Fig. 6. Deviation from ground truth before denoising (top) and after denoising (bottom). Note the different scales on the right used for each panels.

D. Data With Low Spatial Resolution

Experimental conditions of PIV experiments may lead to flow estimates with low spatial resolution Fig. 7 shows the application of our approach to such a scenario.

Our approach plausibly fills in the gaps and returns a flow estimate with higher spatial resolution. We point out that the algorithm treats the input data set like any “noisy” vector field without specification of any prior knowledge.

E. Comparison With TV-Denoising

We compared our approach with a state-of-the-art variational denoising method [21], [22] employing total variation (TV) minimization. The ground truth vector field \mathbf{g} depicted in Fig. 5 was chosen as test data. TV-denoising was separately applied to both components $\mathbf{g} = (g_1, g_2)^T$ of the input data. At first glance, the result depicted in Fig. 8 looks similar to both the input and the vector field obtained with our approach (see Fig. 5). Closer inspection, however, reveals that slight TV-denoising creates significant nonphysical flow structures even in this case where the input vector field does not contain noise at all. Fig. 9 shows close-up views of the results for the section of the input field that is marked in the top panel of Fig. 5. The results illustrates that about 30% of TV-denoised vectors have directions opposite to the ground truth flow, while the result returned by our method nearly matches ground truth. Our result does not *exactly* reproduce ground truth due to the

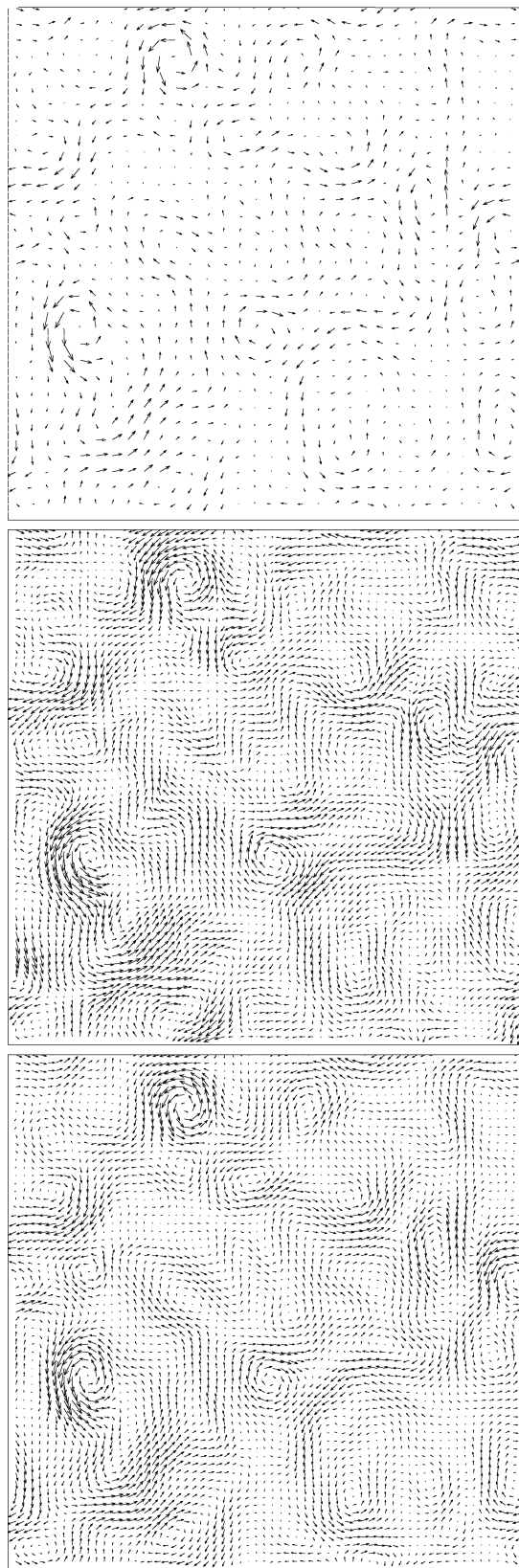


Fig. 7. Top: The data with losses in density. Middle: Restored data. Bottom: Ground truth. Performance measures: SDR = 2.49, ADR = 2.22, NDR = 1.47, DDR = 0.69.

unknown true boundary conditions and due to omitting the time derivative of the vorticity [cf. the discussion in the two

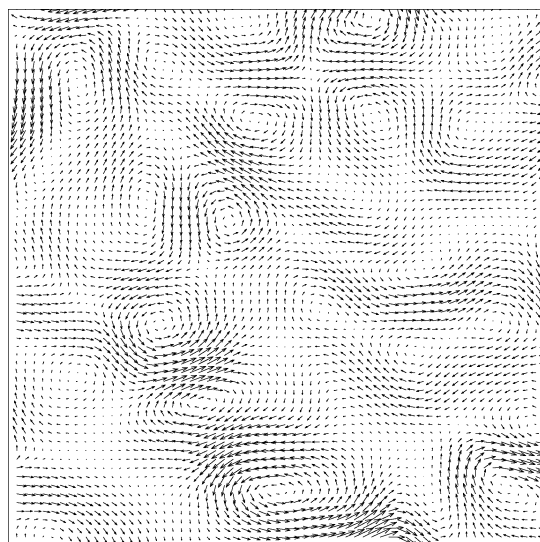


Fig. 8. Vector field resulting from TV-denoising. The corresponding error measurements are SDR = 1.96, ADR = 2.07, DDR = 0.65, NDR = 2.48.

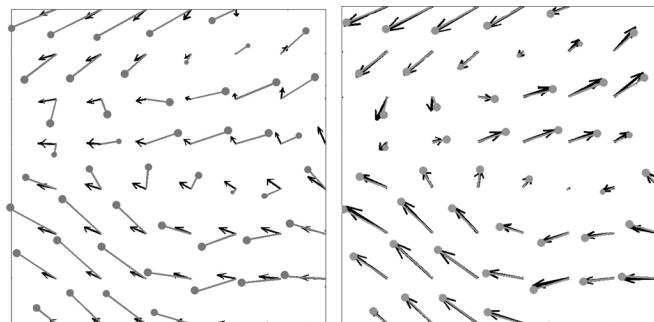


Fig. 9. Left: Close-up view of the result shown in Fig. 8 for the section marked in Fig. 5, top, together with the ground truth vectors (gray vectors with circled heads). Right: The corresponding result of the approach introduced in this paper. TV-denoising (left) cannot preserve physically significant flow structure.

paragraphs following (14)]. Fig. 9, right panel, however, shows that these errors are small.

F. Experiment With Real Data

We applied our approach to real data obtained from PIV measurements of a turbulent boundary layer flow [23]. Fig. 10 shows a velocity field estimate and the corresponding vorticity (represented in gray values; the quantitative meaning of these gray-values in units of sec^{-1} is plotted on the right), computed with commercial software. Though the flow's general structure can be visually recognized, details are perturbed by noise.

The restored velocity vector and vorticity fields are depicted in Fig. 11. Comparing Figs. 10 and 11 reveals that vortices, which are hardly recognized in the input data (see regions $[x = 12, y = 15] - [x = 21, y = 20]$, $[x = 0, y = 30] - [x = 5, y = 40]$) become clearly visible after restoration. For example, the group of outliers in region $[x = 19, y = 24] - [x = 21, y = 26]$ is effectively denoised. Note that the input vector field exhibits abrupt changes and discontinuities, violating the incompressibility constraint (2). Our approaches smoothes such flows so as to yield a physically plausible approximation of the input data.

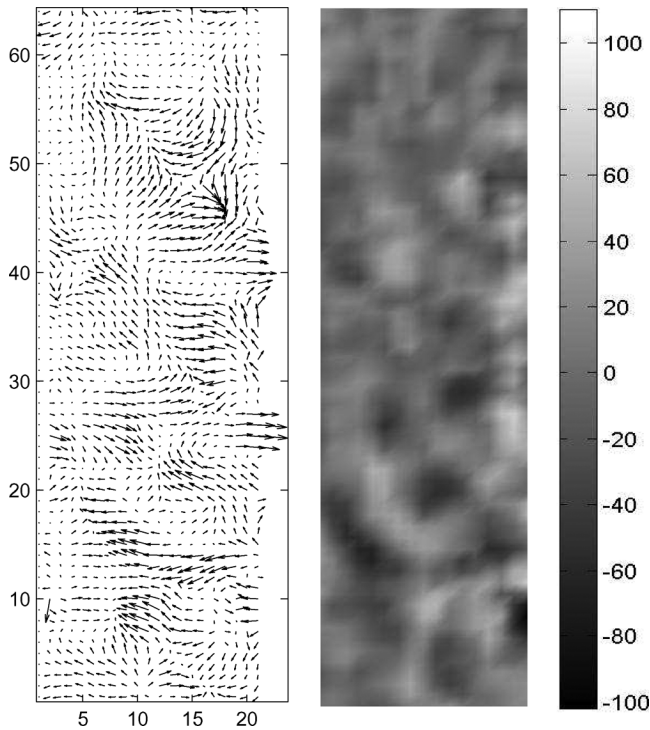


Fig. 10. Measured data. Left: Velocity vector field. Right: Vorticity field.

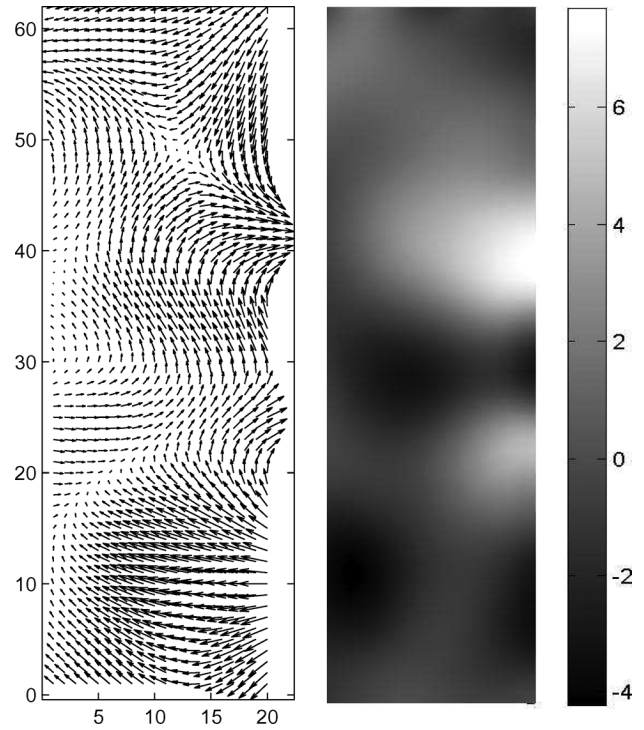


Fig. 12. TV-based data reconstruction. Left: Velocity vector field. Right: Vorticity field.

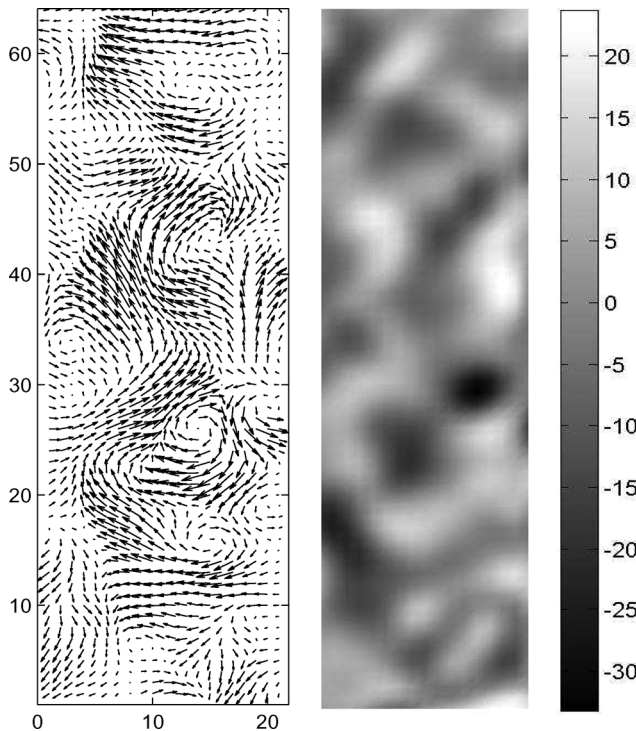


Fig. 11. VTE-based data restoration. Left: Velocity vector field. Right: Vorticity field.

We also applied TV denoising to these real data. The result is shown in Fig. 12. Although it looks smooth, it bears only little resemblance to the input vorticity and velocity vector fields. While the large scale parts exhibit similar structures, the vorticity field looks completely different.

IV. CHOICE OF PARAMETER VALUES

A. Parameter ν in (12)

This parameter has a physical interpretation. It corresponds to the laminar viscosity of the flow under consideration. Depending on the application, its value can be increased, leading to an increased smoothing by linear diffusion of the vorticity field ω minimizing (12).

B. Parameters α and β

Parameter α determines the influence of the residual in the correction step (14). Empirically, $\alpha = \beta = 1$ turned out to be a reasonable choice in (16). These values were used in *all* experiments.

C. Parameter σ

Parameter σ describes the cutoff-frequency of the lowpass filtering step, as described in Section II-D. Although “the best” value depends on the particular data at hand, a broad range of reasonable, save values exist that lead to good performance of the overall algorithm.

To illustrate this point, we repeated the experiment discussed along with Fig. 5 using two extreme values of parameter σ . Fig. 13, top panel, shows the result for the very large value $\sigma = 20$. Obviously, essential parts of the flow pattern shown in the middle panel (ground truth) have been blurred. The result for an opposite extreme value $\sigma \ll 1$ is shown in the bottom panel in Fig. 13. Noise significantly affects the solution, yet all flow structures are visible.

As a consequence, our default choice $\sigma = 1.34$ explained in Section II-D effectively filters out noise—cf. Fig. 5, bottom

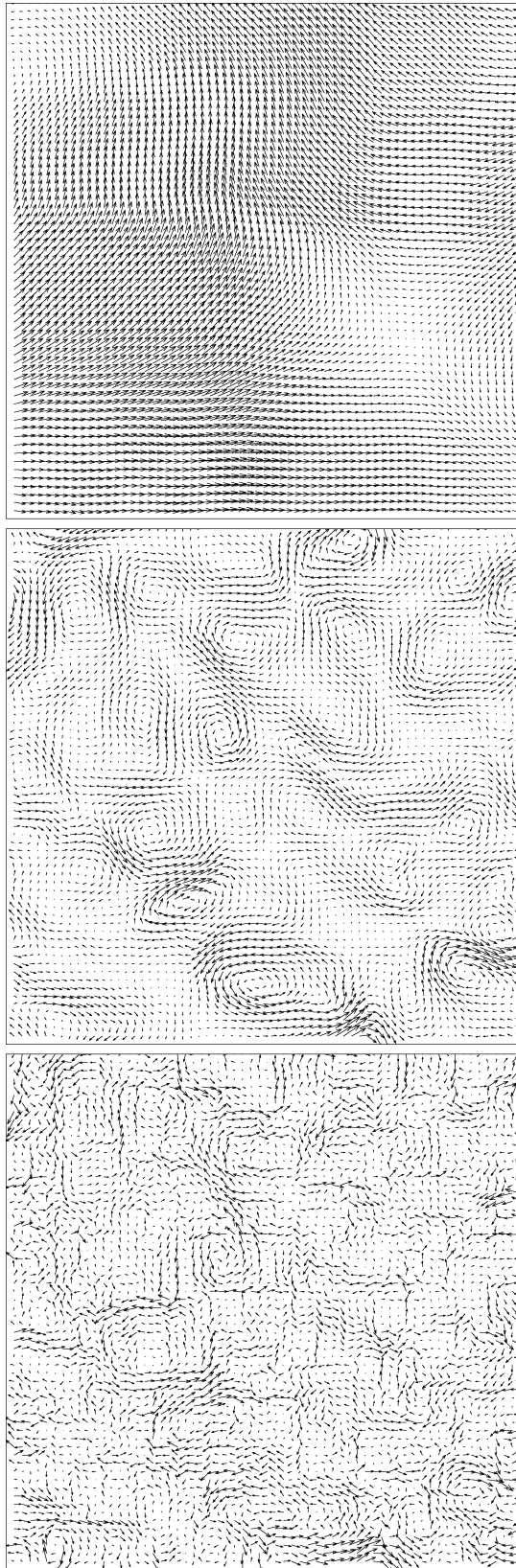


Fig. 13. Top: Output field obtained with $\sigma = 20$. Middle: Ground truth. Bottom: Vector field denoised with $\sigma = 0.1$.

panel—and appears to be a reasonable and robust choice for a broad range of applications.

V. CONCLUSION

We presented an approach for denoising fluid flow estimates obtained from images sequences in experimental fluid dynamics. Prominent features of the approach include (i) that prior knowledge about the physical structure of admissible vector fields is used for restoration, rather than modeling noise explicitly, and (ii) that four computationally simple steps are involved.

A consequence of (i) is broad applicability to scenarios where fluid flow estimates are corrupted in various ways. This was confirmed and demonstrated by numerical experiments using ground truth data and various error types. A consequence of (ii) is a fast processing speed in 2-D, and the applicability to large 3-D problems.

Our future work concerns an evaluation of the method for 2-D problems in collaboration with groups working directly in the field of experimental fluid dynamics, and the application to 3-D tomographic fluid flow measurement [13].

ACKNOWLEDGMENT

The authors would like to thank B. Wieneke, LaVision GmbH, for providing real data sets.

REFERENCES

- [1] C. Tropea, A. L. Yarin, and J. F. Foss, Eds., *Springer Handbook of Experimental Fluid Mechanics*, Springer, 2007.
- [2] A. Vlasenko and C. Schnörr, "Physically consistent variational denoising of image fluid flow estimates," in *Proc. Pattern Recognition 30th DAGM Symp.*, 2008, vol. 5096, LNCS, pp. 406–415.
- [3] R. J. Adrian, "Twenty years of particle velocimetry," *Exp. Fluids*, vol. 39, no. 2, pp. 159–169, 2005.
- [4] M. Raffel, C. E. Willert, S. T. Wereley, and J. Kompenhans, *Particle Image Velocimetry—A Practical Guide*. New York: Springer, 2007.
- [5] F. Brezzi and M. Fortin, *Mixed and Hybrid Finite Element Methods*. New York: Springer, 1991.
- [6] C. Brückner, "Digital-particle-image-velocimetry (DPIV) in a scanning light-sheet: 3D starting flow around a short cylinder," *Exp. Fluids*, vol. 19, no. 4, 1995.
- [7] J. E. Fowler and L. Hua, "Wavelet transforms for vector fields using omnidirectionally balanced multiwavelets," *IEEE Trans. Signal Process.*, vol. 50, pp. 3018–3027, 2002.
- [8] S. Burgmann, C. Brückner, and W. Schröder, "Scanning PIV measurements of a laminar separation bubble," *Exp. Fluids*, vol. 41, no. 2, pp. 319–326, 2006.
- [9] K. D. Hinsch, "Holographic particle image velocimetry," *Meas. Sci. Technol.*, vol. 13, pp. 61–72, 2002.
- [10] H. G. Maas, A. Gruen, and D. Papantoniou, "Particle tracking velocimetry in three-dimensional flows," *Exp. Fluids*, vol. 15, no. 2, pp. 133–146, 1993.
- [11] K. Hoyer, M. Holzner, B. Lüthi, M. Guala, A. Liberzon, and W. Kinzelbach, "3D scanning particle tracking velocimetry," *Exp. Fluids*, vol. 39, no. 5, pp. 923–934, 2005.
- [12] P. Ruhnau, C. Güttler, T. Putze, and C. Schnörr, "A variational approach for particle tracking velocimetry," *Meas. Sci. Technol.*, vol. 16, pp. 1449–1458, 2005.
- [13] G. Elsinga, F. Scarano, B. Wieneke, and B. van Oudheusden, "Tomographic particle image velocimetry," *Exp. Fluids*, vol. 41, no. 6, pp. 933–947, 2006.
- [14] T. Corpetti, E. Mémin, and P. Pérez, "Dense estimation of fluid flows," *IEEE Trans. Patt. Anal. Mach. Intell.*, vol. 24, no. 3, pp. 365–380, Mar. 2002.
- [15] P. Ruhnau, T. Kohlberger, H. Nobach, and C. Schnörr, "Variational optical flow estimation for particle image velocimetry," *Exp. Fluids*, vol. 38, pp. 21–32, 2005.
- [16] T. Corpetti, D. Heitz, G. Arroyo, E. Mémin, and A. Santa-Cruz, "Fluid experimental flow estimation based on an optical-flow scheme," *Exp. Fluids*, vol. 40, no. 1, pp. 80–97, 2006.

- [17] R. Dautray and J.-L. Lions, *Mathematical Analysis and Numerical Methods for Science and Technology*. New York: Springer, 2000, vol. 3.
- [18] C. A. N. Kolmogorov, *C.Roy. Acad. Sci. USSR*, vol. 30, p. 301, 1941.
- [19] P. Ruhnau and C. Schnörr, "Optical Stokes flow estimation: An imaging-based control approach," *Exp. Fluids*, vol. 42, pp. 61–78, 2007.
- [20] P. Ruhnau, A. Stahl, and C. Schnörr, "Variational estimation of experimental fluid flows with physics-based spatio-temporal regularization," *Meas. Sci. Technol.*, vol. 18, pp. 755–763, 2007.
- [21] L. Rudin, S. Osher, and E. Fatemi, "Nonlinear total variation based noise removal algorithms," *Phys.*, vol. 60, pp. 259–268, 1992.
- [22] A. Chambolle, "An algorithm for total variation minimization and applications," *J. Math. Imag. Vis.*, vol. 20, pp. 89–97, 2004.
- [23] A. Schroeder, R. Geisler, K. Staack, B. Wieneke, G. E. Elsinga, F. Scarano, and A. Henning, "Lagrangian and Eulerian views into a turbulent boundary layer flow using time-resolved tomographic PIV," presented at the 14th Int. Symp. Applications of Laser Techniques to Fluid Mechanics, Lisbon, Portugal, Jul. 7–10, 2008.



Andrey Vlasenko received the M.S. degree in applied physics and mathematics from the Moscow University of Physics and Technology in 2006. He is currently pursuing the Ph.D. degree in variational imaging methods using physical prior knowledge.

He joined the IPA group and worked within the German Priority Program "Image Measurements in Experimental Fluid Mechanics" on variational imaging methods using physical prior knowledge. His research interests include computational and experimental fluid dynamics and related methods of

computational data analysis.

Christoph Schnörr received the degrees in electrical engineering and computer science (1987, 1991, 1998) from the University of Karlsruhe, Germany, and the University of Hamburg, Germany, respectively.

He is a Full Professor (University of Mannheim 1999, University of Heidelberg 2008), heading the Image and Pattern Analysis Group and co-directing the Heidelberg Collaboratory for Image Processing (HCI), jointly funded by the German Science Foundation (DFG) and industrial partners. His research interests include image processing, computer vision and pattern analysis, and corresponding problems of mathematical modeling and optimization.